# Supporting Information

## Rational Tailoring of $ZnSnO_3/TiO_2$ Heterojunctions with Bioinspired Surface Wettability for High-Performance Humidity Nanosensors

*Zhenyi Zhang,[a] Jindou Huang,[a] Bin Dong,*[a] Qing Yuan,[a] Yangyang He[a] and Otto S. Wolfbeis[b]*

*[a] Key Laboratory of New Energy and Rare Earth Resource Utilization of State Ethnic Affairs Commission, Dalian Nationalities University, 18 Liaohe West Road, Dalian 116600, P. R. China.*
E-mail: dong@dlnu.edu.cn; Tel. 8641187556959

*[b] Institute of Analytical Chemistry, Chemo- and Biosensors, University of Regensburg, D-93040 Regensburg, Germany*

### Experimental

*Fabrication of $TiO_2$ nanofiber backbones:* $TiO_2$ nanofibers were fabricated through electrospinning with post-calcination. In a typical procedure, 2.0 mL of tetrabutyl titanate ($Ti(OC_4H_9)_4$) was added to a mixture solution containing of 2 mL of acetic acid and 5 mL of ethanol under vigorous stirring. Then, 0.4 g of poly (vinyl pyrrolidone) (PVP) powder (Mn=1300K) were dissolved in the above solution with vigorous stirring for 6 h. Subsequently, the precursor solution was transferred into a plastic syringe with a stainless steel needle (23-gauge) for electrospinning. The distance between the needle tip and the collector was ~10 cm, and the feeding rate was 2.0 $mL{\cdot}h^{-1}$. The dense web of the electrospun nanofibers of PVP/$Ti(OC_4H_9)_4$ composite was fabricated at an applied electric voltage of 10 kV between the needle tip and the collector. Finally, the above composite nanofibers were calcined in air at 500 ˚C with a rising rate of 2 ˚$C{\cdot}min^{-1}$ and kept for 2h at the required temperature. Thus, the $TiO_2$ nanofibers were successfully fabricated.

*Controllable assembly of $ZnSnO_3$ branchs on $TiO_2$ backbones:* One-dimensional $ZnSnO_3/TiO_2$ branched hierarchical heterostructures were synthesized through a glucose-assisted hydrothermal process in which the glucose could serve as the template and/or ligament to guide the $ZnSnO_3$ nanostructure with tailorable feature. In a typical procedure, 0.05 g of the as-electrospun $TiO_2$ nanofibers were dispersed in the 20 mL of premade aqueous solution containing 1.0 mmol of $Zn(CH_3COO)_2{\cdot}2H_2O$, 1.0 mmol of $SnCl_4{\cdot}5H_2O$, 12 mmol

of NaOH, and a certain amount of glucose. After stirring for 30 min, the above mixture was transferred into a Teflon-lined stainless steel autoclave with a capacity of 25 mL. Afterward, the autoclave was sealed and maintained at 180 ℃ for 12 h in an electric oven. After hydrothermal reaction, the autoclave was air-cooled to room temperature. The white suspension was collected, washed with ethanol and deionized water several times, and finally dried in an electric oven at 40 ℃ for a night. Thus, the $ZnSnO_3/TiO_2$ heterostructures with the different kinds of $ZnSnO_3$ secondary nanostructures were synthesized, for which the 0.069, 0.138, and 0.276 mmol of glucose were used to tailor the $ZnSnO_3$ with the nanosphere, nanorod, and nanoneedle structure.

**Characterization**

X-ray diffraction (XRD) measurements were carried out by using Shimadzu XRD-600 X-ray diffractometer with a Cu Kα line of 0.1541 nm. Field emission scanning electron microscopy (FESEM; JSM-7600F) and transmission electron microscopy (TEM; JEOL JEM-2100) were used to characterize the morphologies and structures of the products. Energy dispersive X-ray spectroscopy attached on SEM and TEM was used to analyze the composition of products. Fourier transform infrared (FT-IR) spectra were obtained on a Magna 560 FT-IR spectrometer with a resolution of 1 $cm^{-1}$. X-ray photoelectron spectroscopy (XPS) was performed on a VG-ESCALAB LKII instrument with a Mg Kα ADES ($h\nu$=1253.6 eV) source at a residual gas pressure below $10^{-8}$ Pa. The specific surface areas of the products were measured with a Micromeritics ASAP-2020 instrument and analyzed by the Brunauer–Emmett–Teller (BET) method. A 300-Watt Xe lamp (HSX-F300, Beijing NBET Technology Co. Ltd.) coupled with different bandpass filters (315±10 nm and 550±10 nm) were used to provide the light sources.

**Humidity sensing measurements:**

The sensor manufacturing process and test system are similar to the *Li*'s report.[1] To obtain the humidity nanosensors, The above synthesized $ZnSnO_3/TiO_2$ heterostructures were mixed with ethanol in a weight ratio of 100:10 to form a paste. The paste was coated onto a ceramic substrate with four pairs of Ag-Pd interdigital electrodes to make the film as thin as possible. Finally, the fabricated humidity nanosensor was dried in an electric oven at 60 ℃ for 2 h. The humidity testing system was used a ZL-5 model LCR analyser (made in Shanghai, China). The controlled humidity environments were obtained through the supersaturated

aqueous solutions of different salts in which LiCl, $MgCl_2$, $Mg(NO_3)_2$, NaCl, KCl, and $KNO_3$ in a closed glass vessel at room temperature (25 ℃) produced 11 %, 33 %, 54 %, 75 %, 85 %, and 95 % relative humidity (RH) above the aqueous solutions, respectively.

**Theoretical calculations:**

All of the calculations were implemented in the Vienna ab initio Simulation Package (VASP) code [*Kresse G, Hafner J. Phys Rev B, 1993, 47, 558; Kresse G, Furthmuller J. Phys Rev B, 1996, 54, 11169*]. The geometry optimization is performed using the frozen-core projector-augmented-wave (PAW) method and the generalized gradient approximation (GGA) for exchange correlation [*Perdew J P, Burke K, Ernzerhof M. Phys Rev Lett, 1996, 77, 3865*]. The cutoff energy for the plane-wave basis set is 500 eV and the force on each atom is converged to 0.01 eV/Å; and a set of 6 × 6 × 6 Monkhorst-Pack special k-points and a set of 4 × 4 × 1 Monkhorst-Pack special k-points [*Monkhorst H J, Pack J D. Phys Rev B, 1976, 13, 5188*] have been used for structural relaxations of cell and slab models, respectively. The workfunction calculations were performed on a periodic 1 × 1 unit cell, and a 6 × 6 × 2 Monkhorst-Pack *k*-point grid was used to sample the surface Brillouin zone accordingly. The $TiO_2$ and $ZnSnO_3$ surfaces were modeled with a three-layer slab model with a 50 Å vacuum between any two successive atomic slabs. The calculations of $TiO_2$ and $ZnSnO_3$ surfaces were investigated by employing the range-separated hybrid Heyd-Scuseria-Ernzeh (HSE06) [*Krukau A V, Vydrov O A, Izmaylov A F, Scuseria G E. J Chem Phys, 2006, 125, 224106*] of exchange and correlation functional, which has proven to be a very good method for molecular systems and has recently been applied successfully to the study of $TiO_2$ systems and other systems involving strongly localized d electrons [*Journal of Natural Gas Chemistry 21, 2012, 302–307; International Journal of Hydrogen Energy, 37, 2012, 17870-17881*]. The HSE06 functional is a screened exchange functional, and we set the range separation parameter (μ) to 0.2 $Å^{-1}$. At short range a mixing of 25% of exact Hartree-Fock (HF) and 75% of Perdew-Burke-Ernzerhof (PBE) exchange is used, while at long range the standard PBE exchange is maintained.

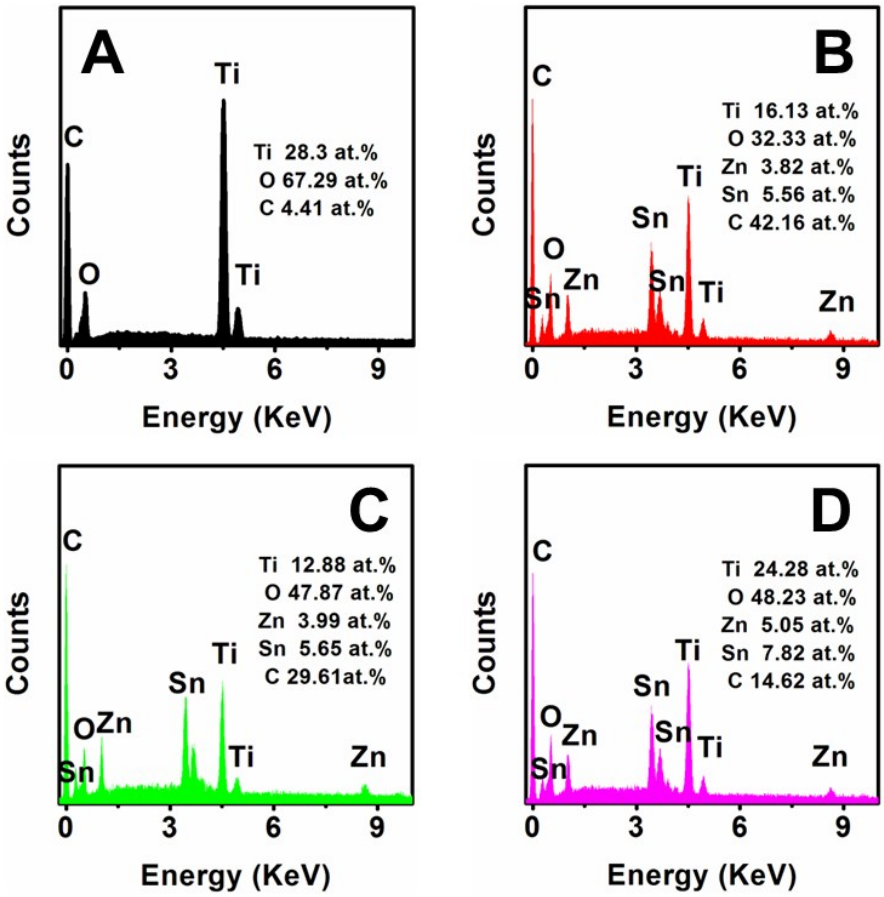


**Figure S1.** Energy dispersive X-ray spectroscopy from the corresponding SEM images; spectrum A from Figure 1A; spectrum B from Figure 1B; spectrum C from Figure 2B; spectrum D from Figure 2C.

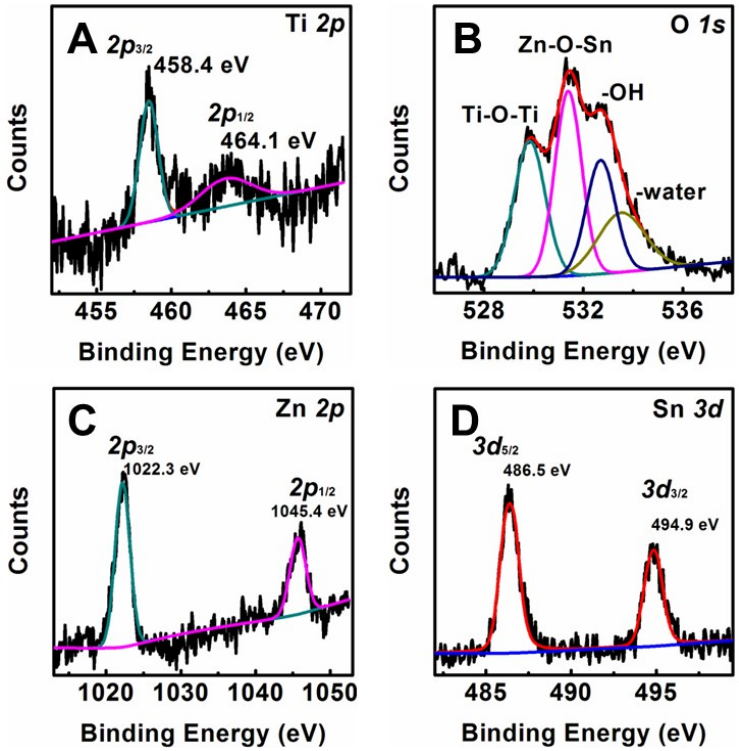


**Figure S2.** X-ray photoelectron spectroscopy (XPS) spectra of the as-synthesized $ZnSnO_3$ nanoneedles/$TiO_2$ nanofibers heterojunction: (A) Ti 2p core-level spectrum; (B) O 1s core-level spectrum; (C) Zn 2p core-level spectrum; (D) Sn 3d core-level spectrum.

As observed in Figure S5 A, the spin-orbit splitting between Ti $2p_{3/2}$ and Ti $2p_{1/2}$ for the hierarchical nanostructures are about 5.7 eV, indicating that the valence state of Ti was +4.[2] Meanwhile, the O 1s signal can be fitted into four symmetric peaks (Figure S5 B), in which the peaks located around 529.8, 531.38, 532.68, and 533.59 eV are attributed to the crystal lattice oxygen for Ti-O-Ti, Zn-O-Sn, surface hydroxyl groups (-OH), and surface-adsorbed water molecules of hierarchical nanostructures, respectively.[2] Figures S5 C shows typical Zn $2p_{3/2}$ and $2p_{1/2}$ transitions. The peaks at 1022.3 and 1045.4 eV with the observed spin-orbit splitting energy of 23.1 eV are responsible for the $Zn^{2+}$ ions in the $ZnSnO_3$ nanocrystals.[3] Meanwhile, the peaks located at 486.5 and 494.9 are ascribed to the Sn $3d_{5/2}$ and Sn $3d_{3/2}$ of $Sn^{4+}$, respectively.[2] The above results further confirmed that the hierarchical nanostructures consisted of $ZnSnO_3$ and $TiO_2$.

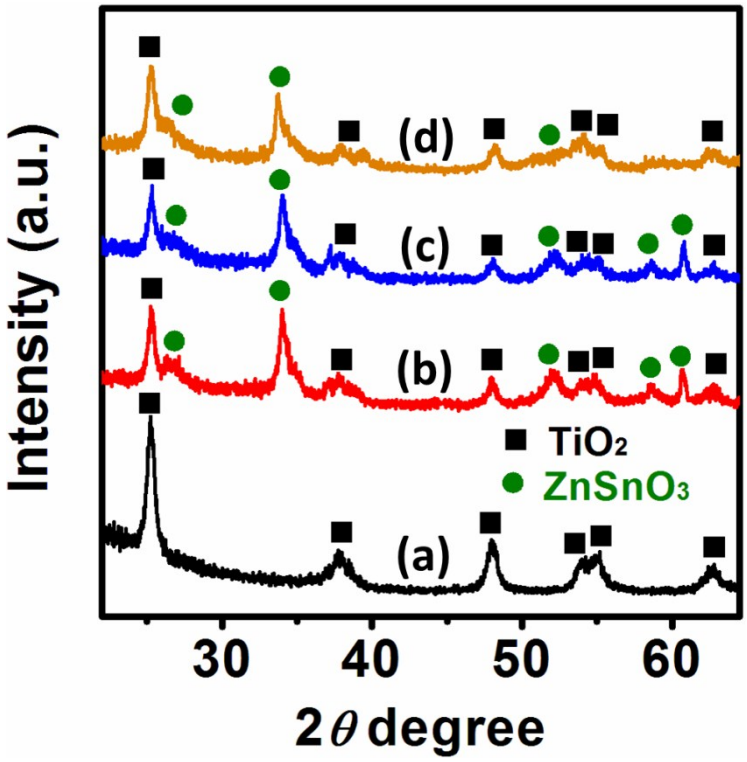


**Figure S3.** X-ray diffraction (XRD) patterns of the as-synthesized samples: (a) $TiO_2$ nanofibers; (b) $ZnSnO_3$ nanoneedles/$TiO_2$ nanofibers heterojunction; (c) $ZnSnO_3$ nanorods/$TiO_2$ nanofibers heterojunction; (d) $ZnSnO_3$ nanoparticles/$TiO_2$ nanofibers heterojunction.

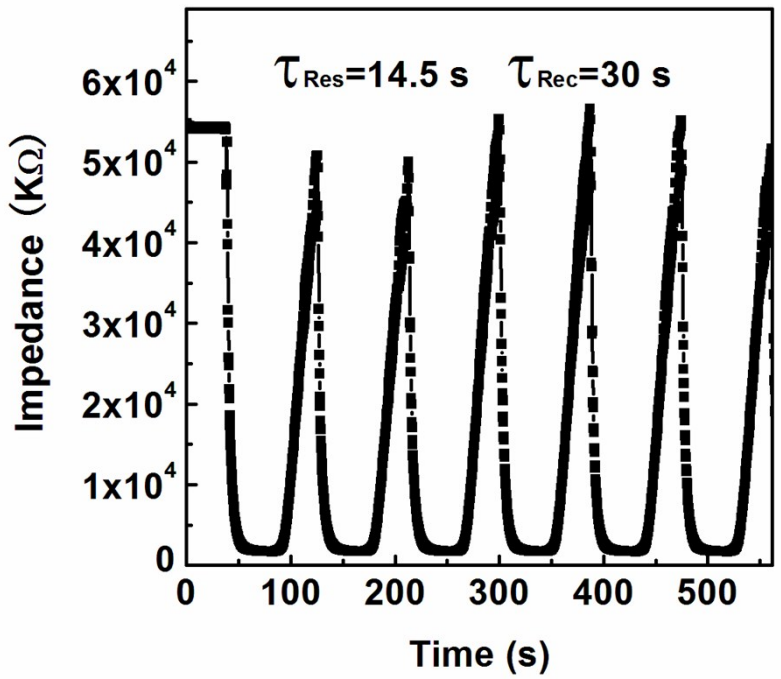


**Figure S4.** Response and recovery characteristic curves based on the nanosensors containing $ZnSnO_3$ nanoparticles.

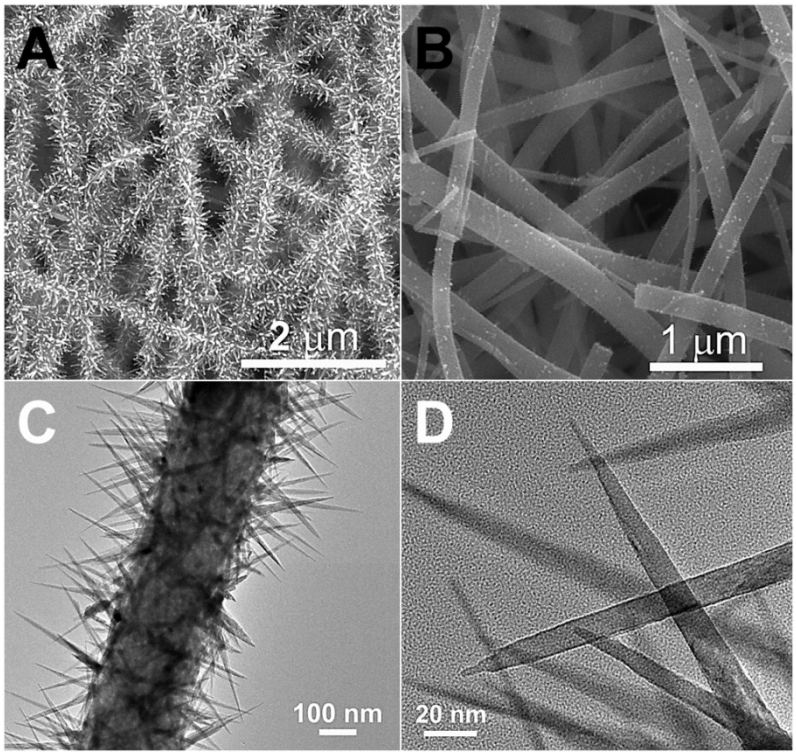


**Figure S5.** (A) Scanning electron microscopy (SEM) image of $ZnSnO_3$ nanoneedles/$TiO_2$ nanofibers heterojunction; (B) SEM image of $TiO_2$ nanofibers after hydrothermal treatment in the absence of glucose template and/or ligament, showing that the high density of secondary nanostructures can not be obtained on the $TiO_2$ nanofibers; (C) Transmission electron microscopy (TEM) image of an individual $ZnSnO_3$ nanoneedles/$TiO_2$ nanofiber heterojunction; (D) TEM image of the $ZnSnO_3$ nanoneedles.

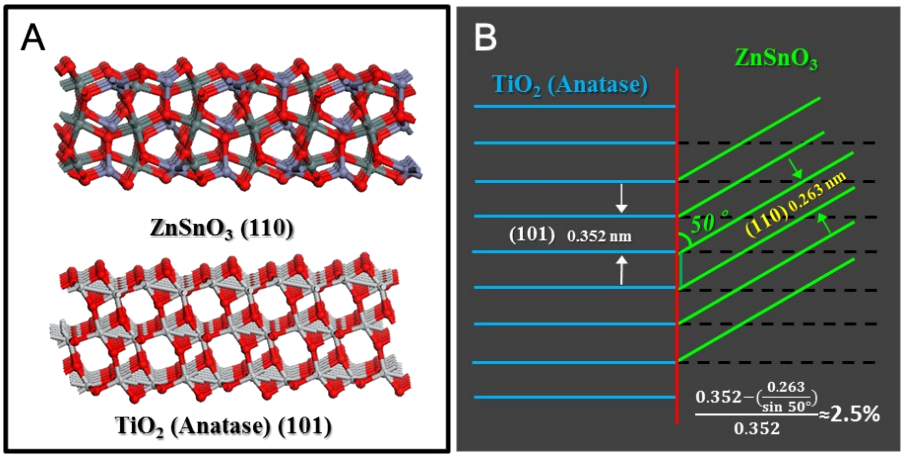


**Figure S6.** (A) Structural model of the atomic arrangement on the (110) plane of $ZnSnO_3$ and (101) plane of $TiO_2$; (B) Schematics of the heterojunction interface between the (110) plane of $ZnSnO_3$ and (101) plane of $TiO_2$, suggesting their low interfacial lattice mismatch.

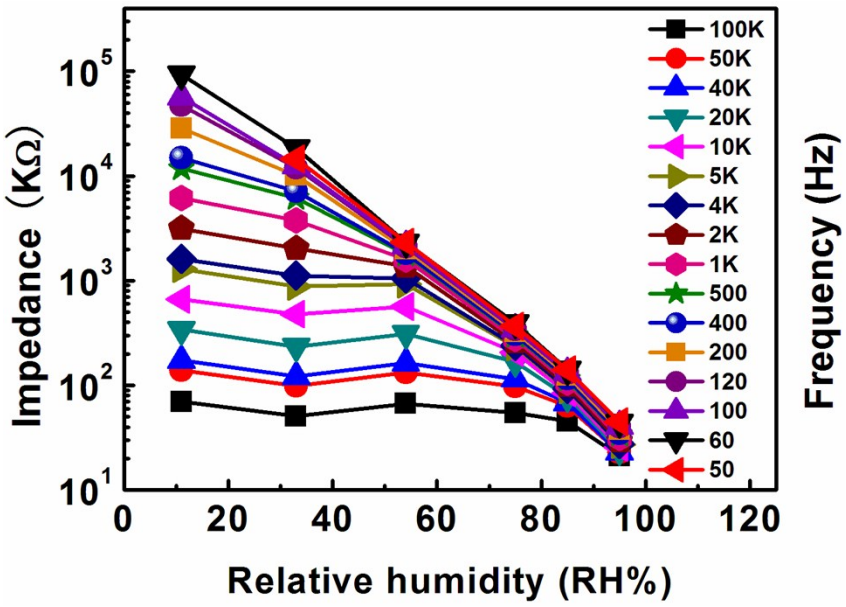


**Figure S7.** Relationship of impedance and relative humidity (RH) based on the $ZnSnO_3$ nanoneedles/$TiO_2$ nanofibers heterojunction at different frequencies.

The humidity sensing tests were performed on a series of nanosensor devices produced by the as-synthesized samples. The applied AC voltage was 1 V. Figure S6 shows the relationship between the impedance and RH based on the $ZnSnO_3$ nanoneedles/$TiO_2$ nanofibers heterojunction by adjusting the operation frequency. It is proven that the best linearity between the impedance and RH can be achieved by operating an appropriate frequency at 100 Hz. Thus, the following sensing tests were performed at this frequency.

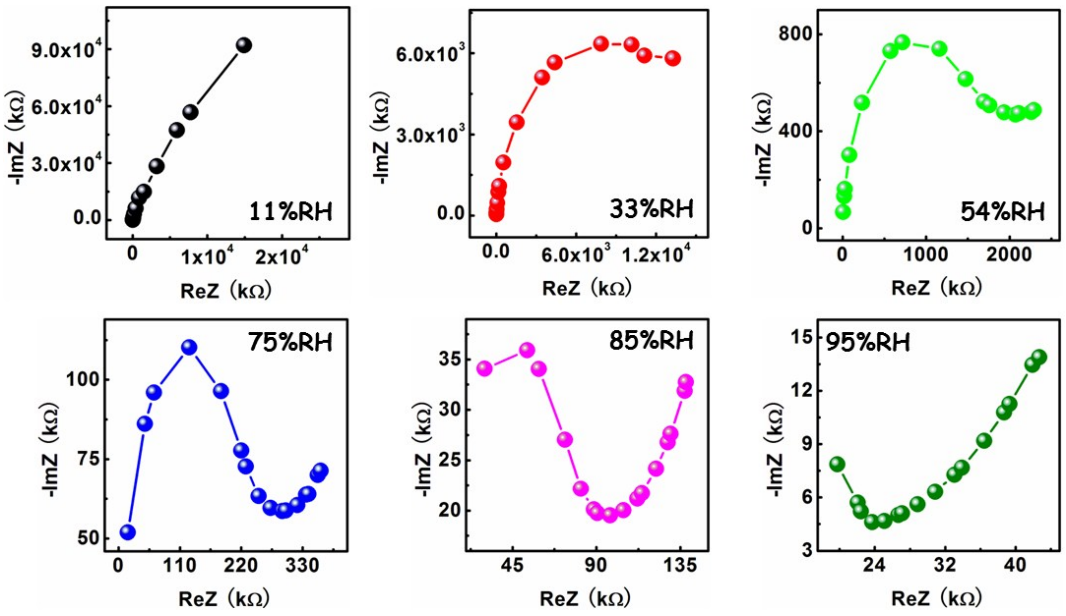


**Figure S8.** Complex impedance plots of the as-fabricated nanosensor based on $ZnSnO_3$ nanoneedles/$TiO_2$ nanofibers heterojunction at different relative humidity.

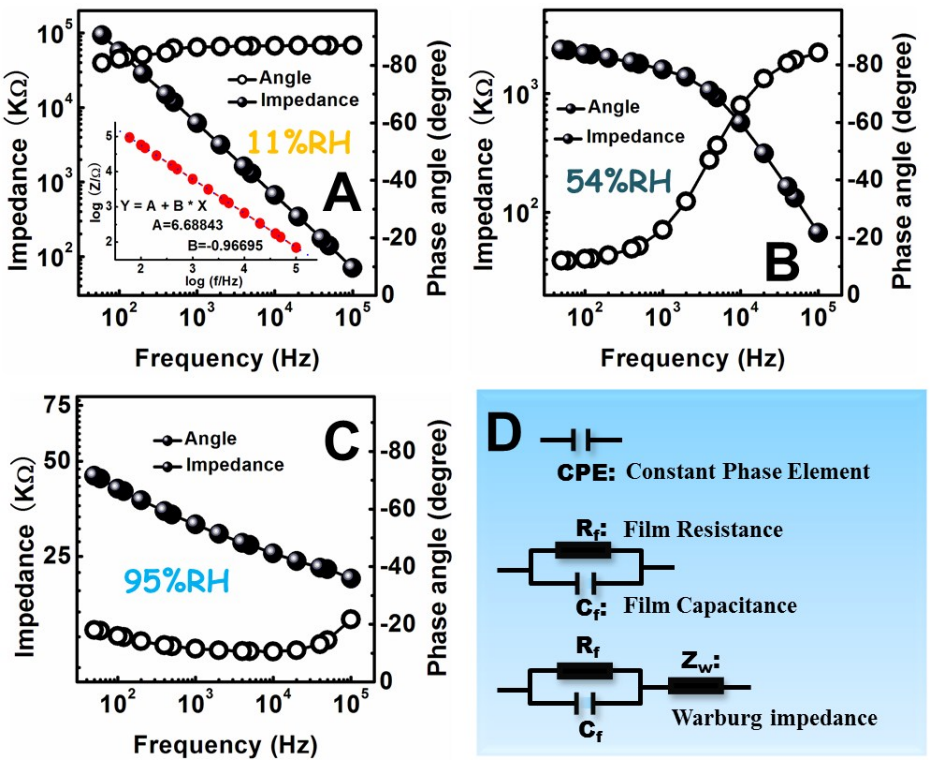


**Figure S9.** Bode diagrams of the as-fabricated nanosensor based on $ZnSnO_3$ nanoneedles/$TiO_2$ nanofibers heterojunction at the RH of (A) 11%, (B) 54%, and (C) 95%; (D) Equivalent circuits of the nanosensor in the corresponding RH environment.

The complex impedance plots measured by adjusting the operation frequency form 50 Hz to 100 KHz under the different RH were also used to research the humidity sensing behaviors of the $ZnSnO_3/TiO_2$ hierarchical heterostructures. As observed in Figure S7, the complex impedance curves of $ZnSnO_3$ nanoneedles-based heterostructures change from a straight line to quasi-semicircles and to semicircle together with the straight lines (or a straight lines after the half semicircle), when the humidity environment is shifted from low RH (11%) to medium RH (33%, 54%), and to high RH (75%, 85%, 95%). Apparently, the equivalent circuits can be modeled by three types, shown in the Figure S8 D. At 11% RH, the phase angle is nearly constant when the frequency shifts from 50 Hz to 100 KHz. Meanwhile, the impedance is decreased with the increase of frequency. So the equivalent circuit at this RH can be described by a constant phase element (CPE) as follow:[4] $|Z_{CPE}| = \frac{\omega^{-n}}{Y_0}$, where $\omega = 2\pi f$, $f$ frequency, $Y_0$ a real parameter, and $n$ a real parameter whose value can vary from 0 (pure resistor) to 1 (pure capacitor). Taking the logarithm on both sides of the above equation, we can obtain another equation:[5] $\log|Z_{CPE}| = -n\log f + \log\frac{1}{(2\pi)^n Y_0}$. The $n$ value in our case can be estimated from a plot of $\log|Z_{CPE}|\ VS.\ \log f$. As can be seen in the insert of Figure S8 A, the $n$ value is 0.967, suggesting that the nanosensor becomes an almost pure capacitor. In the middle RH at 54%, the impedance also decreases as increasing of the frequency. However, the phase angle is increased with the frequency and approaches to -90° . Thus, the relationship between phase angle and frequency can be deduced by the equation ( $\varphi = arc\tan\omega RC$) based on the equivalent circuit consisting of a resistor ($R_f$) and a capacitor ($C_f$) connected in parallel. It is obviously that when the frequency approaches to be infinite, the phase angle should approaches to -90° . When RH rises to 95%, the impedance also decreases as increasing of the frequency (Figure S8 C). However, the phase angle is decreased at low frequency, and increased at high frequency. Furthermore, the complex impedance plot at this RH shows a shorter line in high frequency and a longer line in low frequency. The shorter line is part of a semicircle, which is ascribed by a resistor ($R_f$) and a capacitor ($C_f$). The longer line represents Warburg impedance ($Z_w$) originated from the protons diffusion process. Thus, these observations indicate that the equivalent circuit is comprised of $R_f$, $C_f$, and $Z_w$. Moreover, the impedance is mainly dominated by the $Z_w$.

**References:**

[1] Z. Li, H. Zhang, W. Zheng, W. Wang, H. Huang, C. Wang, A. G. MacDiarmid, Y. Wei, *J. Am. Chem. Soc.* **2008**, *130*, 5036.

[2] Z. Zhang , C. Shao, X. Li, Y. Sun, M. Zhang, J. Mu, P. Zhang, Z. Guo, Y. Liu, *Nanoscale* **2013**, *5*, 606.

[3] Z. Zhang, C. Shao, X. Li, L. Zhang, H. Xue, C. Wang, Y. Liu, *J. Phys. Chem. C* **2010**, *114*, 7920.

[4] S. Borini, R. White, D. Wei, M. Astley, S. Haque, E. Spigone, N. Harris, J. Kivioja, T. Ryhänen, *ACS Nano* **2013**, *7*, 11166.

[5] W. Geng, Q. Yuan, X. Jiang, J. Tu, L. Duan, J. Gu, Q. Zhang, *Sens. Actuators B* **2012**, *174*, 513.